Journal of Solid State Chemistry 181 (2008) 1915–1924

Contents lists available at ScienceDirect

Journal of Solid State Chemistry

journal homepage: www.elsevier.com/locate/jssc

Solid-state NMR and EPR study of fluorinated carbon nanofibers

Wei Zhang [a], Marc Dubois [a,*], Katia Guérin [a], André Hamwi [a], Jérôme Giraudet [b], Francis Masin [b]

[a] Laboratoire des Matériaux Inorganiques, UMR CNRS 6002-Clermont Université, 24 av. des Landais, 63177 Aubière Cedex, France
[b] Matière Condensée et Résonance Magnétique, Université Libre de Bruxelles (U. L. B.), CP 232, Boulevard du Triomphe, B-1050 Bruxelles, Belgium

ARTICLE INFO

Article history:
Received 20 February 2008
Received in revised form
18 March 2008
Accepted 30 March 2008
Available online 10 April 2008

Keywords:
Carbon nanofibers
Fluorination
Nuclear magnetic resonance (NMR)
Electron paramagnetic resonance (EPR)

ABSTRACT

Carbon nanofibers were fluorinated in two manners, in pure fluorine gas (direct fluorination) and with a fluorinating agent (TbF_4 during the so-called controlled fluorination). The resulting fluorinated nanofibers have been investigated by solid-state nuclear magnetic resonance (NMR) and electron paramagnetic resonance (EPR). This underlines that the fluorination mechanisms differ since a $(CF)_n$ structural type is obtained, whatever the temperature, with the controlled reaction, whereas, during the direct process, a $(C_2F)_n$ type is formed over a wide temperature range. Through a careful characterization of the products, i.e. density of dangling bonds (as internal paramagnetic centers), structural type (acting on molecular motion) and specific surface area (related to the amount of physisorbed O_2), the effect of atmospheric oxygen molecules on the spin-lattice nuclear relaxation has been underlined.

1. Introduction

Due to their numerous applications, such as electrode in primary lithium batteries, solid lubricants, storage reservoir for strong oxidant and fluorinating agent (BF_3, ClF_3), fluorinated carbons have, during the last decades [1–8], been extensively studied. In each application, the chemical, electrochemical and tribological properties depend strongly on both the nature of the C–F bonding (within the fluorocarbon matrix) and the involved structural type, i.e. $(CF)_n$, $(C_2F)_n$ or fluorine-GIC $(C_xF)_n$. In particular and because of their high discharge potential (up to 2.4 V) and high specific capacity (up to 800 mA h g^{-1}) [8,9], fluorinated carbons are commonly used as cathode in non-aqueous primary lithium batteries. When carbon nanofibers (CNFs) are used as precursor, a specific power of 8000 W kg^{-1} and a maximum of 6 C of current density have been obtained. This is because insulating fluorinated parts are closely mixed, at nanoscale, to conductive non-fluorinated carbons [10].

High-resolution solid-state nuclear magnetic resonance (NMR) is a well-adapted technique for the study of fluorinated graphite fluorides and fluorine graphite intercalation compounds [4,11–19]. Both the intercalated species (containing ^{19}F and ^{1}H nuclei for example) and the fluorocarbon matrix (^{19}F and ^{13}C) can specifically be identified [11,14,19]. In particular, the ^{13}C and ^{19}F spin-lattice relaxation times T_1 are quite useful in establishing fluorination mechanisms and also in identifying the type of fluorinated carbons formed during the process. For instance, covalent $(CF)_n$-and $(C_2F)_n$-type graphite fluorides exhibit different ^{19}F T_1 values, at 282 MHz, close to 450 and 210 ms [15,18]. Our previous studies revealed that physisorbed paramagnetic oxygen acts both in nuclear and in electron resonances [15,16]. This results in changes of the ^{19}F nuclear spin-lattice relaxation time, T_1, which significantly increases when the oxygen molecules were removed from the sample surface. In the case of covalent $(CF)_n$, the T_1 values were 0.45 s in presence of O_2 and 10.10 s after its removal upon out-gassing [15]. This O_2 effect depends on the specific surface area (SSA) of the solid i.e. on the amount of physisorbed oxygen.

Other effects also regulate magnetic relaxation [20]. They are as follows:

(i) Molecular motions related to structural parameters, for instance, the stacking of fluorocarbon sheets gives rise to structural defects, such as CF_2 and CF_3 groups, and dangling bonds (DB).
The measured ^{19}F T_1 obtained using IF_5 catalyst and post-treated at 530 °C is 595 ms in air atmosphere [18]. For a conventional covalent $(CF)_n$ ($T_1 = 450$ ms), the presence of a molecular motion having an activation energy of 1.169 kJ mol^{-1} has been found [15] and shown to be compatible with a simple C–F bond oscillation.
(ii) The presence of internal paramagnetic centers (PC) (which, in the case of fluorinated carbons, are often DB having a localized spin). Panich [11] found, at 44 MHz, a shorter T_1 for $(C_2F)_n$

* Corresponding author. Fax: +33 4 73 40 71 08.
E-mail addresses: wei.zhang@univ-bpclermont.fr (W. Zhang), marc.dubois@univ-bpclermont.fr (M. Dubois), katia.guerin@univ-bpclermont.fr (K. Guérin), andre.hamwi@univ-bpclermont.fr (A. Hamwi), jerome.giraudet@ulb.ac.be (J. Giraudet), fmasin@ulb.ac.be (F. Masin).

0022-4596/$ - see front matter © 2008 Published by Elsevier Inc.
doi:10.1016/j.jssc.2008.03.037

(53 ms) than for $(CF)_n$ (400 and 660 ms for samples prepared starting from petroleum coke and natural graphite, respectively) and attributed this difference to the presence of PC [11,12]. The effect of PC on nuclear spin relaxation has been the subject of many studies [21–23] and results from a coupling between nuclear spin and unpaired electrons (even when the latter are in very small concentration because, compared with nuclei, electrons have a much larger gyromagnetic ratio). The internal PC are either DB having a localized electron whatever the fluorinated carbon [12,24–26] and spin carriers due to the charge transfer between the residual catalysts [27,28]).

The various contributions to the spin-lattice relaxation times make the comparison between different fluorinated carbons very difficult; all contributions depend on the starting carbonaceous material, structural order, initial granulometry, surface properties, dimensionality (graphite, nanotube and fullerene) and fluorination method (duration, fluorinating agent, and temperature). The particular example of $(CF)_n$ underlines the difference between the various T_1 values found in the literature: 400 and 660 ms at 44 MHz for samples prepared starting from petroleum coke and natural graphite, respectively [11,18]. At 282 MHz, the values for the same samples are 450 (coke) and 785 ms (graphite).

In this work, in addition to the study of the fluorination processes, we focus on the effect of adsorbed oxygen molecules on the magnetic nuclear relaxation in fluorinated CNFs. All these samples present an identical structural phase. Their electronic spin density (D_S) (formed only by DB [29]) only slightly changes upon fluorination. On the other hand, their SSAs, i.e. B.E.T. surfaces, change with the fluorination temperature and F:C molar ratio; this results in a large variation of the amount of physisorbed O_2 molecules. This allows us to examine this particular point of the effect of absorbed O_2 on T_1 without having to consider major changes of the other parameters (molecular motion, density of PC). The first part will be devoted to a comparison between samples obtained using either F_2 gas (direct fluorination) or a fluorinating agent, terbium tetrafluoride (TbF_4), (controlled fluorination). The presence of paramagnetic oxygen will be confirmed by electronic paramagnetic resonance. Finally, the evolution of spin-lattice relaxation times as a function of SSA will be discussed.

2. Experimental

2.1. Synthesis and chemical composition of the fluorinated carbons nanofibers

High-purity (>90%) CNFs, 2–20 μm in length, were supplied by courtesy of the MER Corporation, Tucson, Arizona. They were obtained by chemical vapor deposition (CVP) and heat treated at 1800 °C in an argon atmosphere to enhance their graphitization degree. The well-defined periodicity of the layers was confirmed both by transmission electron microscopy and X-ray diffraction (interlayer distance $d = 0.337$ nm). The diameter distribution is between 80 and 350 nm. The average diameter ($\langle \Phi \rangle$) is estimated equal to 150 nm from observations of various parts of the raw sample.

Two types of fluorinated CNFs have been studied. The first was synthesized by direct fluorination in pure F_2 gas for temperatures T_F ranging between 380 and 480 °C; the corresponding materials will be named **D**-T_F. Details on synthesis and direct fluorination mechanism have been already published elsewhere [29]. A second batch was synthesized using a fluorinating agent, TbF_4; its thermal decomposition generates mainly atomic fluorine $F^\bullet$ rather than molecular fluorine F_2 [30]. TbF_4 was obtained in pure F_2 gas at 500 °C starting from TbF_3 (Aldrich, 99.9%). Its purity (i.e. the absence of residual TbF_3) was systematically checked by X-ray diffraction. A thermogravimetric analysis of TbF_4, run till 350 °C, indicated that exactly one mole of $F^\bullet$ was released per mole of TbF_4 between 100 and 300 °C. This experiment was carried out under argon flow in order to avoid the formation of oxyfluorides.

For the CNFs fluorination with TbF_4 (denoted **C**-T_F), a closed reactor was used in order to preserve the defined fluorine amount (atomic and/or molecular) released by the thermal decomposition of TbF_4. A two temperatures oven was used: the part containing TbF_4 was heated at 450 °C whatever the experiment whereas CNFs were heated at temperatures T_F between 420 and 500 °C.

A reaction time of 16 h was used. Prior to heating, a primary vacuum ($\sim 10^{-2}$ atm) was set in the reactor. The reactions involved during the fluorination are the following:

$$TbF_4 \xrightarrow{\Delta} TbF_3 + F^\bullet \quad \text{or/and} \quad \tfrac{1}{2}F_2 \tag{1}$$

$$C + xF^\bullet \quad \text{or/and} \quad \frac{x}{2}F_2 \rightarrow CF_x \tag{2}$$

An excess of TbF_4 (1.5 times the stoichiometric values) was used in each case. The total conversion of TbF_4 into TbF_3 was checked by both weight loss and X-ray diffraction analysis.

The F:C molar ratio of fluorinated CNFs was determined by quantitative ^{19}F NMR measurements (Table 1). The static spectra of the samples and of polyvinyldifluoride $(CF_2–CH_2)_n$, which was used as a reference, were recorded with similar receiver gain, scan number and recycling time D_1 ($D_1 > 5T_1$ using the longest spin-lattice relaxation times T_1 in air atmosphere, which corresponds to **C**-420 and **D**-480, so $D_1 = 5$ and 3 s for **C**-T_F and **D**-T_F, respectively). The intensities are divided by the sample mass. This method has been successfully checked with two conventional $(CF)_n$ samples of compositions $CF_{1.1}$, $CF_{1.0}$, obtained by direct reaction of natural graphite and petroleum coke, respectively, with fluorine gas at 600 °C, and a $(C_2F)_n$ sample of composition $CF_{0.6}$, obtained by direct reaction of natural graphite with fluorine gas at 380 °C.

2.2. Physico-chemical characterizations

Nitrogen adsorption isotherms were measured at 77 K by a Micromeritics ASAP 2020 automatic apparatus. Before measurements, samples were pre-treated under secondary vacuum at 300 °C during 2 h for sufficient removal of impurities.

Electron paramagnetic resonance (EPR) spectra were run using a X band Bruker EMX spectrometer operating at 9.653 GHz at room temperature. Diphenylpicrylhydrazyl was used to calibrate the resonance frequency ($g \approx 2.0036 \pm 0.0002$) and densities of spins carriers D_s. Data processing and simulations were performed using Bruker WIN-EPR and SimFonia software, respectively.

NMR experiments were carried out with a Bruker Avance spectrometer, at working frequencies for ^{13}C and ^{19}F of 73.4 and 282.2 MHz, respectively. A Magic Angle Spinning probe (Bruker) operating with a 4 mm rotor was used. For MAS spectra, a simple sequence was performed with a single $\pi/2$ pulse length of 4 and 3.5 μs for ^{19}F and ^{13}C, respectively. Spin-lattice relaxation time T_1 was measured using a saturation recovery sequence. The $\pi/2$ pulse width was between 1 and 5 μs.

NMR experiments were also performed at higher frequency on a Tecmag spectrometer (working frequency for ^{19}F 470.7 MHz). A special Cross Polarization/Magic Angle Spinning probe (Doty) with fluorine decoupling on a 4 mm rotor was used. The ^{19}F $\pi/2$ pulse width was 3 μs. High MAS spinning speeds, 35 and 70 KHz, were also performed with Bruker probe on a Bruker spectrometer (working frequency for ^{19}F 470.7 MHz).

Table 1
Physico-chemical data of the fluorinated CNFs as a function of the fluorination conditions

Sample	T_F (°C)	F:C	% sp^2 Carbon atoms	$D_s \times 10^{19}$ (spin g^{-1})	SSA ($m^2 g^{-1}$)	Air	T_1 (ms) (±5) vacuum	Vacuum+air
D-390	390	0.08	–[a]	5.0±1.0	24.0±0.5	492		
D-405	405	0.15	–[a]	7.8±1.6	30.2±0.5	254		
D-420	420	0.39	82	9.3±1.9	65.1±0.6	223	885	
D-428	428	0.59	26	16.2±3.2	93.7±0.7	230		
D-435	435	0.68	25	16.4±3.3	110.5±0.8	232		
D-450	450	0.74	20	24.9±5.0	112.9±0.8	243		
D-472	472	0.90	10	24.3±4.9	111.1±0.7	320		
D-480	480	1.04	9	77.3±15.5	139.8±0.5	417	709	
C-420	420	0.12	87	5.2±1.0	50.9±0.5	906	1580	824
C-450	450	0.56	46	3.3±0.7	104.8±0.7	565		
C-480	480	0.70	35	5.5±1.1	102.7±0.5	541	1540	498
C-500	500	0.91	20	8.1± 1.6	137.2±0.7	444		

[a] Cannot be estimated.

^{13}C and ^{19}F chemical shift were externally referenced to tetramethylsilane (TMS) and CF_3COOH, respectively. ^{19}F chemical shift were referenced with respect to $CFCl_3$ ($\delta_{CF_3COOH} = -78.5$ ppm vs. δ_{CFCl_3}).

Scanning electron micrographs (SEM) were recorded using a Cambridge Scan 360 SEM operating at 3 kV. Transmission electron microscopy was performed with FEI CM200 operating at 200 kV. The CNFs were dispersed in chloroform using ultrasonic treatment and a few drops of suspension were deposited onto copper observation grids covered with ultrathin carbon/formvar films. The grids were subsequently dried at ambient conditions.

3. Results and discussion

3.1. Fluorination mechanisms

^{19}F and ^{13}C solid-state NMR results (Figs. 1 and 2) show that the mechanisms of the two fluorination routes are different. The ^{19}F chemical shift ($\delta_{^{19}F}$) of the main NMR line (Fig. 1a) observed whatever the fluorination condition indicates that the C–F bonding is covalent. This is because the observed $\delta_{^{19}F}$ is equal to −190 ppm/$CFCl_3$ close to the one for covalent graphite fluorides [11–19]. This C–F bonding implies that the carbon hybridization is mainly sp^3. On the other hand, compared with direct fluorination, the TbF_4 route generates lower surface disorder and lower structural defects, which consist of CF_2 and CF_3 groups located on the sheet edges. As a matter of fact, for the direct fluorination sample, the presence of a second isotropic line at −120 ppm (its first spinning sideband is visible as a shoulder on the C–F isotropic line) indicates the presence of CF_2 groups. Their amount is small but sufficient to be detected by ^{19}F MAS NMR. The content of CF_2 is generally well correlated with the amount of CF_3 groups. CF_3 are also detected by several narrow lines which are present in the −60/−90 ppm range in the case of the direct fluorination and superimposed with spinning sidebands of C–F and CF_2 lines. These groups can be localized on the fluorocarbon sheet edges and probably rotate rapidly around the C–C bonds, explaining the narrowness of their resonance line.

High field measurements (at 470.7 MHz) were also carried out in order to better separate the various contributions. ^{19}F NMR spectra of fluorinated CNFs (**D**-480, **D**-472 and **C**-500) were recorded with MAS, spinning rates of 15 KHz (Fig. 1b), 35 and 70 KHz (Fig. 1c).

As expected due to an improved homogeneity of the magnetic field and a better resolution of the line, the increase of the working frequency from 282.2 to 470.7 MHz results in a significant narrowing of the CF_2 line. On the contrary, the full width at half maximum (f.w.h.m.) is still constant for C–F line whatever the working frequency (f.w.h.m. ≈4700 Hz).

The linewidth of the C–F line could result from an envelop of several lines with close chemical shifts rather than one contribution.

Due to a better resolution of the various lines, except C–F line, these experiments allow the various chemical shifts to be confirmed: −190, −126 and −86 ppm for C–F, CF_2 and CF_3 groups, respectively. When two samples of similar fluorine content are compared, i.e. 0.90 and 0.91 for **D**-472 and **C**-500, respectively, the amounts of CF_2 and CF_3 groups are lower for the sample prepared by the controlled route. Another difference appears with a working frequency of 470.7 MHz by the presence, for **D**-472 only, of an additional shoulder at −180 ppm on the isotropic line of C–F bonds (Figs. 1b and c). This line has never been observed for covalent fluorinated carbons and its origin is unclear.

Its chemical shift of −180 ppm indicates carbon–fluorine interaction lower than in covalent C–F bond ($\delta_{^{19}F} = -190$ ppm). It is to note that "semi-covalent" C–F bond, i.e. the bonding due to the hyperconjugation involving C–C bonds into the carbon sheets and C–F bonds, results in the lowering of the C–F bonding order [6] and exhibits a chemical shift of −170 ppm [31]. Taking into account ^{13}C NMR data of CNFs fluorinated by F_2 at 472 °C [29] and by TbF_4 at 500 °C (see after) the relative amounts of "semi-covalent" C–F bonds are closed in the two samples. Such an assignment for the additional line is not further retained.

As this line is not present for **D**-480 and **C**-500, which exhibit a $(CF)_n$ type whereas $(C_2F)_n$ is still present in **D**-472, the additional line could be related to the presence of $(C_2F)_n$ phase rather than to structural disorder. The fluorocarbon sheets stacking differs in $(C_2F)_n$ and $(C_2F)_n$ phases and the coexistence of the two phases implies the presence of intermediate regions in the layers, which separated the two phases. We believe that the additional line is assigned to these intermediate regions but this hypothesis remains to be verified by comparing various covalent graphite fluorides obtained by different syntheses.

A major advantage of the process using fluorinating agent is the smaller amount of CF_3 and CF_2 groups as shown by their corresponding NMR lines which are decreased for CF_2 or absent for CF_3 in the spectra of CNFs fluorinated using TbF_4 (except for **C**-480 and **C**-500 for which the CF_3 line is very weak).

The formed fluorinated parts exhibit different structural phase. In the case of direct fluorination $(C_2F)_n$ type is formed in a wide temperature range except at 480 °C where $(CF)_n$ type is also found due to a partial exfoliation of the sample [29]. Only $(CF)_n$ type is formed during the controlled fluorination and this whatever the

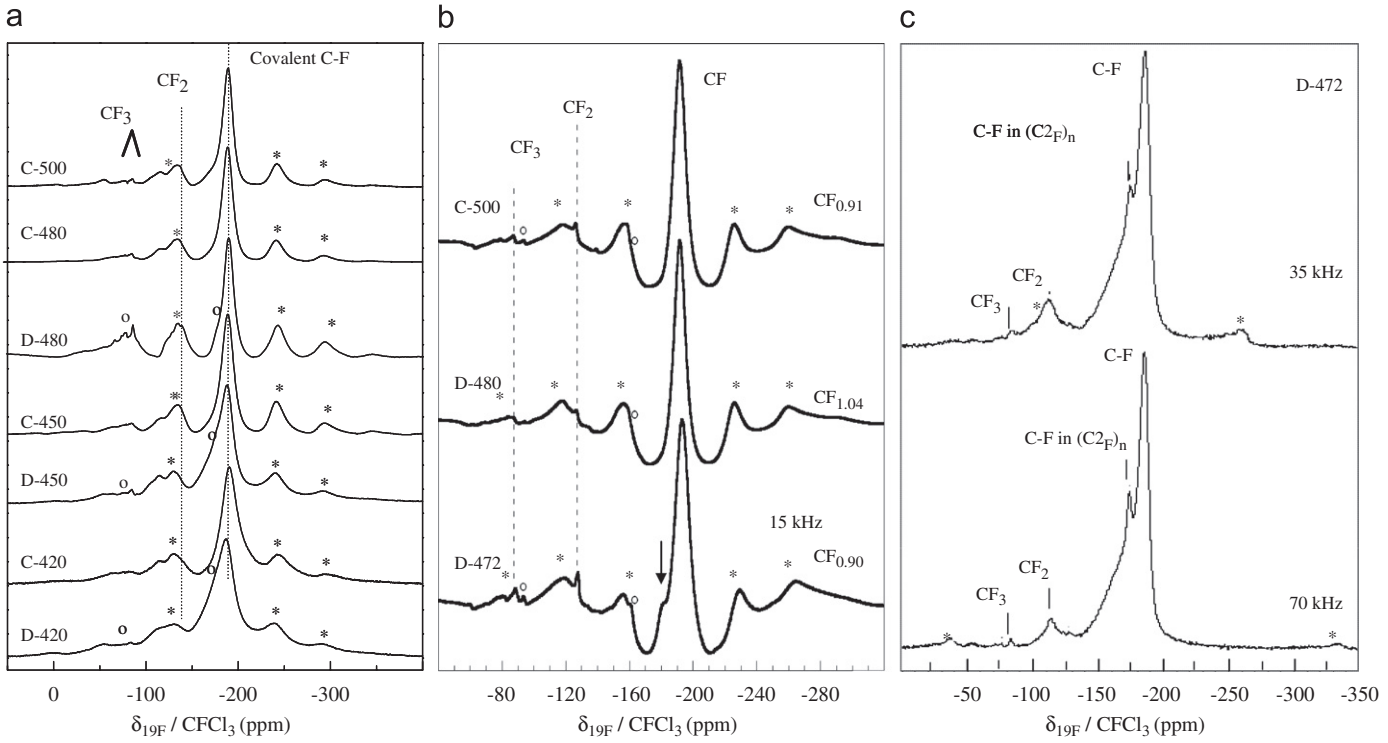

Fig. 1. ^{19}F MAS NMR spectra at 282.2 MHz (a) and at 470.7 MHz (b) and (c); the spinning speeds were 14 KHz (a), 15 KHz (b), 35 and 70 KHz (c). * and ○ denote spinning sidebands.

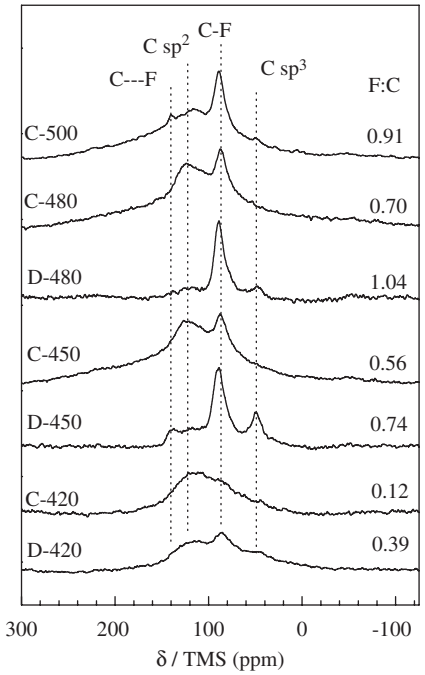

Fig. 2. ^{13}C MAS NMR spectra of the fluorinated CNFs; the spinning speed was 10 kHz.

temperature. As the carbon hybridization is sp^3, the fluorocarbon layers are corrugated in both structural phases and consist of *trans*-linked cyclohexane chairs or *cis–trans*-linked cyclohexane boats. Contrary to $(CF)_n$ in which each carbon atom is covalently bonded to a fluorine atom, in $(C_2F)_n$, pairs of buckled sheets are present and only half of the carbon atoms are fluorinated. In accordance with the structural model presented by Sato et al. [32], every pair of adjacent carbon sheets are bonded to each other by covalent C–C bonds (forming diamond-like carbon atoms). The ^{13}C spectra of $(CF)_n$ and $(C_2F)_n$ types exhibit a common line at 88 ppm/TMS and is assigned to carbon atoms in strong interaction with fluorine, i.e. covalently bonded [4,11,14,15,18,19] (noted C–F in Fig. 2) Moreover, diamond-like carbon atoms, which ensure the connection between the fluorocarbon layers in $(C_2F)_n$ type, results in a ^{13}C chemical shift (δ_{Csp^3}) of 42 ppm, close to the one of pure diamond which is found to be 35 ppm [33]. This line is not significant in the case of CNFs fluorinated using TbF_4 contrary to what is found for the direct route (Fig. 2). In the latter, a $(C_2F)_n$-type structure is present till 472 °C. At higher fluorination temperature, $(C_2F)_n$ is converted into $(CF)_n$ and the relative intensity of the line at 42 ppm decreases for **D**-480. Whatever the fluorination temperature, another broad resonance peak appears at 120 ppm i.e. close to the one of pure graphite, and is therefore assigned essentially to residual graphitic carbons plus a certain amount of sp^2 carbon atoms in weak interaction with fluorine ($\delta_{C\cdots F} = 140$ ppm). Its relative percentage, estimated by spectral fitting, decreases when the fluorination temperature increases and then with the fluorine content. Table 1 summarizes the percentage of the sp^2 carbon atoms estimated by the ratio $S(Csp^2)/[S(Csp^2)+S(C–F)+S(C\cdots F)+S(Csp^3)]$ where S is the area of the line.

The amount of reactive fluorine atoms in the reactor is kinetically controlled for the fluorinating agent TbF_4. TbF_4 is thermally decomposed into TbF_3 with a progressive release of either atomic $F^\bullet$ or molecular F_2 fluorine. This leads to an equilibrium between the two types of fluorine: $2F^\bullet \Leftrightarrow F_2$. Atomic $F^\bullet$ is known to be more reactive than F_2 and therefore constitutes the main fluorinating agent. This displays the equilibrium towards more $F^\bullet$ and allows a higher fluorination level to be obtained, i.e. $(CF)_n$ type even at low temperature. Moreover, fluorination occurs more progressively with lower structural defects.

Selected fluorinated CNFs using both TbF_4 and F_2 were characterized by TEM (Fig. 3, see also Ref. [29]) and SEM (Fig. 4)

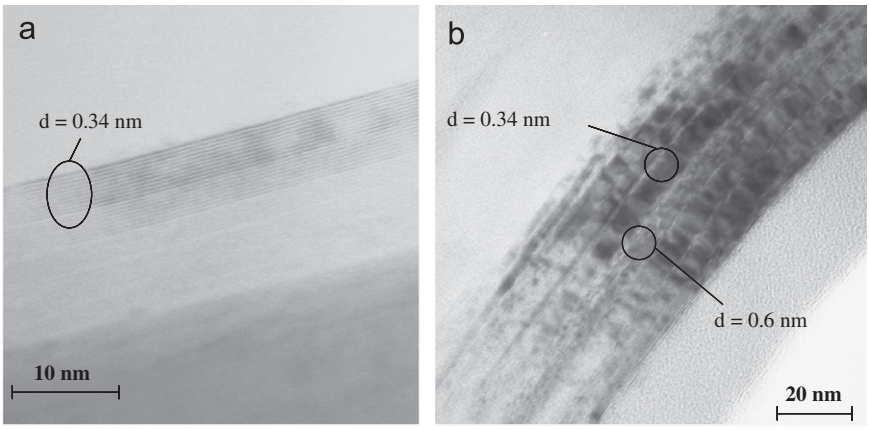

Fig. 3. TEM image of the raw material (a) and of CNFs fluorinated at 480 °C using TbF_4 (b).

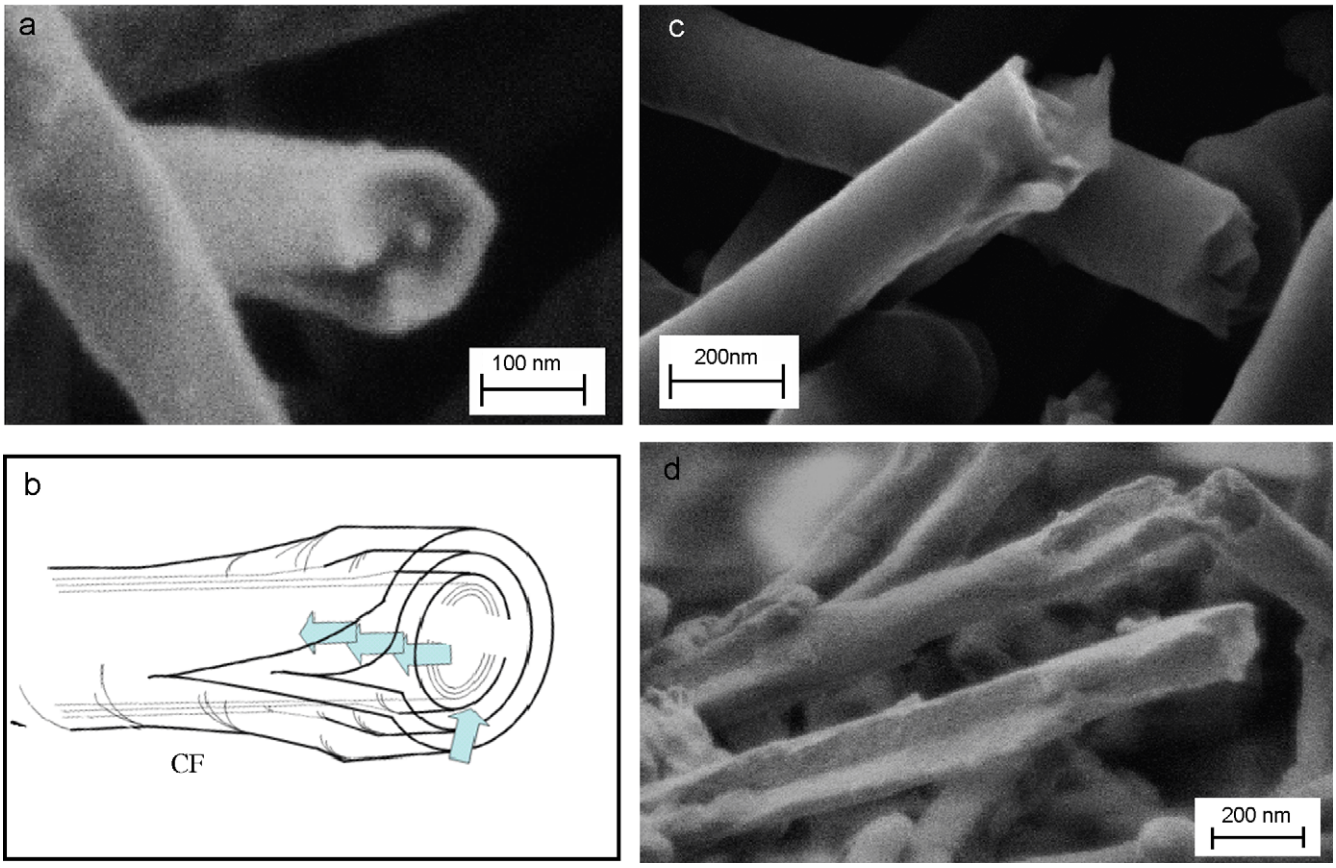

Fig. 4. SEM image of selected fluorinated carbon nanofibers **C**-420 (a) **C**-480 (c) and **D**-480 (d) and (b) schematic illustration of the fluorination mechanism in accordance with reference [34].

allowing the fluorinated parts to be underlined. In these small domains, due to the accommodation of fluorine atoms within the graphene layers, the disorder increases and the interlayer distance increases from the one of raw CNFs (0.34 nm) up to the classical value of $(CF)_n$-type graphite fluoride structure (*d*-spacing equal to 0.60 nm) for the controlled fluorination. Using the direct fluorination, *d*-spacing of the fluorinated layers indicates the formation of $(C_2F)_n$ type. The dispersion of the fluorinated parts depends on the reaction temperature; they are dispersed in the overall bulk at 480 °C (Fig. 4) whereas, for the lower fluorination temperature, at 420 °C for both the direct and controlled fluorinations the distorted layers were located near the nanofiber surface. In the case of the direct fluorination, such disordered layers dispersion has not been observed at 480 °C and some exfoliation occurs [29].

The fluorination starts on the defective or unsaturated carbons sitting at outlayers or the nanofiber tips although their amount is quite low since the sample were post-treated at 1800 °C under argon atmosphere. The fluorination could then progresses toward the core through an opening of some external walls in order to permit the volume expansion resulting from the accommodation of fluorine atoms and the carbon hybridization change from sp^2 into sp^3. SEM image of **C**-420 and **C**-480 in Figs. 4a and c, respectively, supports this proposed model schematically shown in Fig. 4b in accordance with Ref. [34]. Using F_2 gas at

480 °C (Fig. 4d), this process occurs with a partial exfoliation resulting in some cracks due to the expansion.

3.2. EPR study

Fig. 5 displays the EPR spectra of three selected samples, **C**-480, **C**-500 and **D**-480.

It should be noted that no EPR signal is present for pristine CNFs. The origin of the EPR lines is identified as carbon DB having a localized spin. Such spin carriers have been proposed for other fluorinated carbon obtained in F_2 atmosphere [12,14–16,24–26]. Because of the progression of the fluorinated part containing the DB, the larger the F:C ratio, the larger the spin density and thus the higher the intensity of the EPR line (Table 1). The *g*-factor is close to 2.003 ± 0.002 (typical for free radicals and localized structural defects in carbons). Simulation of the spectra reveals that three contributions (Lorentzian) are needed to perfectly fit the spectra of **C**-480, **C**-500 and **D**-480 acquired in ambient air atmosphere (Fig. 5, Table 2). For all fluorinated CNFs, except **D**-480 and **C**-500, the spectra consist of two lines (1 and 2) related to DB having different environments; the peak-to-peak linewidths (ΔH_{pp}) are equal to 6.3 and 14.9 ± 0.2 G (**C**-480). The third line (line 3) is broad ($\Delta H_{pp} = 60 \pm 2$ G), and assigned either to the interaction of the DB with the paramagnetic oxygen molecules (adsorbed on the CNF surface) or to a non-resolved superhyperfine structure (SHFS). This latter results from the hyperfine interaction of the DB with neighboring fluorine nuclei (nuclear spin number $I = 1/2$). For the higher temperature, using direct fluorination (**D**-480) or TbF_4 (**C**-500), this SHFS, due to $n = 6$ ^{19}F nuclei, is resolved resulting in $2nI+1 = 7$ lines (Figs. 5d–f); its origin is probably the higher fluorine content (F:C = 1.04 and 0.91 for **D**-480 and **C**-500, respectively). Simulation of the signal leads to a hyperfine parameter $A = 45 \pm 2$ G, a linewidth $\Delta H_{pp} = 36\,\text{G} \pm 2\,\text{G}$

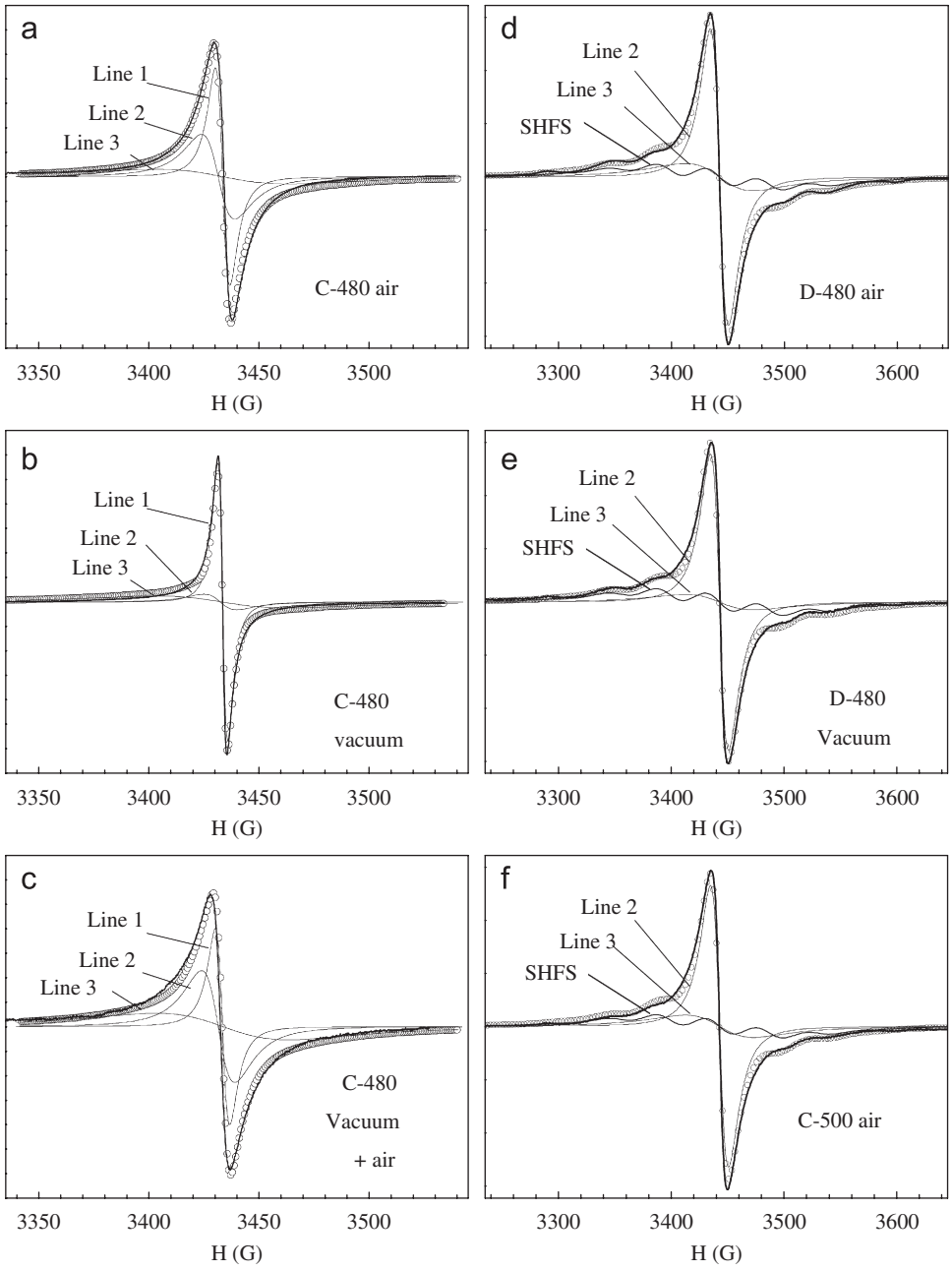

Fig. 5. EPR spectra and simulation of fluorinated CNFs.

Table 2
Parameters of the EPR spectra

	Line 1 ±5 G	Line 2	Line 3	SHFS
C-480 air				
ΔH_{pp} (G)	6.3	14.9	60	–
%S[a]	18.1	34.3	47.6	
C-480 vacuum				
ΔH_{pp} (G)	4.5	14.8	60	–
%S[a]	41.9	24.4	33.7	
C-480 vacuum +air				
ΔH_{pp} (G)	6.5	14.9	60	–
%S[a]	11.0	31.0	58.0	
C-500 air				
ΔH_{pp} (G)		16.2	60	[b]
%S[a]		28.4	28.8	42.8
D-480 air	–			
ΔH_{pp} (G)		15.8	60	[b]
%S[a]		26.4	31.5	42.1
D-480 vacuum	–			
ΔH_{pp} (G)		16.0	60	[b]
%S[a]		30.1	19.9	50.0

[a] $\%S_i = S_i/\sum S_{Lines}$ with S_i the area of the line integral and $\sum S_{Lines}$ the sum of the integral.

[b] Superhyperfine structure (SHFS) with $(2nI+1) = 7$ lines where $n = 6$ is the number of neighboring fluorine nuclei (nuclear spin number $I = \frac{1}{2}$) (coupling constant $A = 45 \pm 2$ G, linewidth $\Delta H_{pp} = 36\,G \pm 2\,G$[16].

and a g-factor of 2.003 ± 0.001. These EPR parameters are close to the ones proposed by Panich et al. [12] who have study fluorinated petroleum cokes and interpreted the large linewidth by the joint effect of dipole–dipole and exchange interactions between PC. For covalent graphite fluoride, similar SHFS has been observed starting from petroleum coke [15,16], natural graphite [18] or room temperature graphite fluorides post-fluorinated at high temperature [14]. In addition to SHFS, the spectra of **D**-480 and **C**-500 only exhibit line 2 ($\Delta H_{pp} = 15.8\,G \pm 0.2$ G and $16.2\,G \pm 0.2$ G, respectively) and 3 ($\Delta H_{pp} = 60\,G \pm 2$ G). The non-resolved hyperfine structure, which was also observed, is due to different configurations of the fluorine atoms surrounding the DB [18]. Comparison of the spin density D_s for the two fluorination routes (Table 1) reveals that the amount of DB at a given fluorination level is lower using the controlled process. D_s slightly increases with temperature except for **D**-480 for which a partial exfoliation occurred resulting in an important increase of the structural defects, in particular the DB.

Interactions between carbon DB and paramagnetic oxygen adsorbed on the surface of CNFs could modify the magnetic properties. This behavior has been already observed for $(CF)_n$ and $(C_2F)_n$ graphite fluorides [15,16] and in conducting polymers such as polypyrrole [35], protonated emeraldine form of polyaniline [36,37] and of polyaniline sulfonate-based hybrid nanocomposite [38]. In order to verify this hypothesis in the present case, EPR spectra of **C**-480 and **D**-480 were recorded after out-gassing for one hour at 120 °C and 2 h at 300 °C under secondary vacuum (Figs. 5b and e, sample **C**-480 vacuum and **D**-480 vacuum). After the out-gassing, the samples are transferred under N_2 and into a quartz EPR tube in a glove box (filled with argon). The EPR tubes are then sealed off. Out-gassing results in the removal of physisorbed molecules from the sample surface, such as atmospheric paramagnetic O_2 and HF molecules. In the case of **C**-480, the spectrum was also recorded after re-exposure to air atmosphere (Fig. 5c, denoted **C**-480 vacuum+air). Taking into account the relative ratio $\%S_i = S_i/\sum S_{Lines}$, where S_i is the area of the line integral for the i signal and $\sum S_{Lines}$ the sum of the area, the out-gassing of **C**-480 leads to a decrease of this ratio for lines 2 and 3 whereas the percentage of the line 1 increases from 18.1% to 41.9% (Table 2). The removal of O_2 molecules from the surface results in the suppression of the interaction between paramagnetic O_2 and DB; this leads to the narrowing of the line from ΔH_{pp} close from 14.9 G (line 2) to 6.3 G (line 1) showing that these two contributions concern similar DB but with different interaction with O_2. This process is reversible since the area ratio after re-exposure to air atmosphere is quite similar to the initial state. Due to the initial presence of HF and H_2O molecules in the sample porosity, the surface properties and the amount of O_2 are not rigorously equal before and after out-gassing explaining why the area ratio slightly differs. In the case of **D**-480, the percentages of SHFS and line 2 increase after out-gassing whereas that of line 3 decreases due to a conversion into SHFS. The presence of O_2 results in an increase of the linewidth for the seven lines of SHFS; this leads to the observed non-resolved SHFS (line 3). EPR clearly underlines the interaction between adsorbed O_2 molecules and DB. O_2 species act as a relaxation agent, which lowers the T_1 spin-lattice relaxation time and/or the T_2 spin–spin relaxation time (which is inversely proportional to the linewidth ΔH_{pp}).

3.3. *Effect of PC and of physisorbed oxygen molecules on nuclear spin-lattice relaxation*

Coupling between nuclear spin and unpaired electron spin, even in small concentration, produces an effective channel for nuclear spin-lattice relaxation. The relaxation behavior depends on the spin diffusion constant. In the case of diffusion limited relaxation, the magnetization $M_z(t)$ possess two different regions: for very short time $M_z(t)$ is proportional to $t^{1/2}$ and proceed asymptotically to an exponential function of time [21]. For a diffusionless process, the growth of magnetization has been shown to be in $t^{1/2}$ for very short time [21], for longer time the magnetizable evolves as $\exp[-(t/T_1)^{1/2}]$ [22,23]. In absence of relaxation by PC or in the case of rapid spin diffusion, $M_z(t)$ follows an exponential function of time for all values of t without the transient region in $t^{1/2}$ [21]. In Fig. 6 are reported the characteristic magnetizable growth (in the form of $[1-M_z(t)/M_{z0})]$ as a function of $t^{1/2}$ for various samples fluorinated at the lowest and highest temperatures (420, 480 and 500 °C). The recovery is linear whatever the sample and for longer time the magnetization is an exponential function of the time. Presence of PC is then a factor of relaxation.

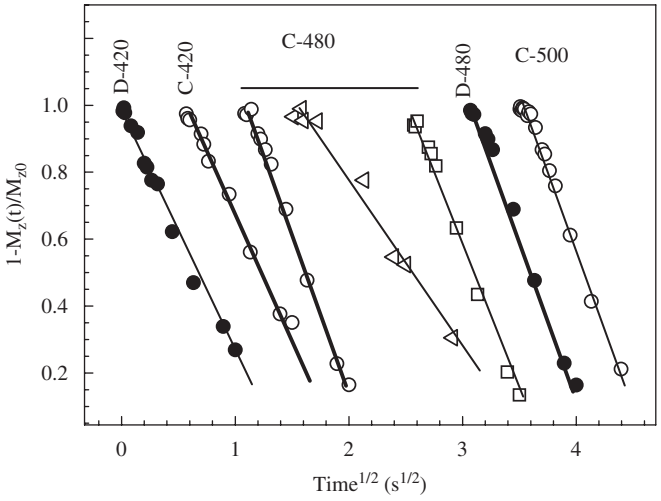

Fig. 6. Initial ^{19}F magnetization curve of fluorinated CNFs, $1-(M_z(t))/M_0$ vs. $t^{1/2}$, in presence of air (○ and ●), after out-gassing (△) and after out-gassing and re-exposure to air (□). ○, △ and □ refer to the sample obtained using the controlled fluorination and ● is used for CNFs fluorinated using F_2. The abscissa has been shifted to separate the curves (0.5 or 1.0 $s^{1/2}$).

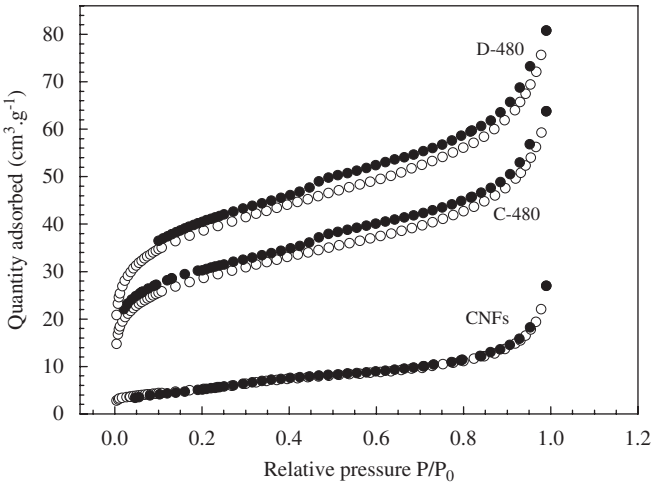

Fig. 7. N_2 adsorption–desorption isotherms at 77 K of raw, **C**-480 and **D**-480. ○ and ● represent the adsorption and desorption curves, respectively.

The following part will focus on the quantification of the effect of paramagnetic O_2 molecules as a function of the small surface area (SSA). First, the surface properties were investigated by nitrogen adsorption at 77 K. The raw CNFs present a low SSA ($18\,m^2\,g^{-1}$); the adsorption and desorption curves are superimposed (Fig. 7). The porosity is essentially interparticular because, whatever the sample, the adsorption data deviate significantly from a flat to a curved feature above $P/P_0 = 0.1$ (above the monolayer formation) indicating uptake on the external surface. Fluorination results in (i) a small ill-defined mesoporosity as revealed by the small hysteresis found between the adsorption and desorption branches, (ii) microporosity is increased as shown by a significant increase of the amount of nitrogen adsorbed in the low relative pressure domain ($P/P_0 < 0.1$). Moreover, the slope after the curvature is more pronounced, indicating the progressive filling of the external surface. This behavior occurs for the two kinds of fluorination; nevertheless, it is more pronounced for direct fluorination than in for the controlled process indicating a larger surface disorder when pure F_2 is used; the SSA (i.e. B.E.T. surface) is also systematically higher for the direct fluorination at the same reaction temperature. For both the controlled and direct fluorination, the evolution of SSA with T_F exhibits three distinct parts:

- The results obtained in the case of direct fluorination at $T_F \leqslant 435\,^{\circ}C$, and for **C**-420 and **C**-450 (Table 1) show that fluorination starts on the nanofibers surface, leading to surface disorder and an opening of the porosity; the SSA increases steadily.
- Between 435 and 472 °C for **D**-T_F and for **C**-480, fluorination progresses towards the core without significant change of the surface, the SSA remains constant.
- Finally, due to the partial exfoliation at higher temperature in F_2 gas [29], the SSA increases once more reaching a value close to $140\,m^2\,g^{-1}$. This process occurs at 480 °C for direct fluorination and at 500 °C in the case of controlled fluorination.

The variation of ^{19}F spin-lattice relaxation with fluorination temperature is shown in Table 1. Rather than T_1 values, Figs. 8a and b show the relaxation rate $R_1 = 1000/T_1$ as a function of fluorination temperature and SSA, respectively. By comparing our results with T_1 values of well-known graphite fluorides, $(CF)_n$ and $(C_2F)_n$ types, it is possible to extract some structural-type

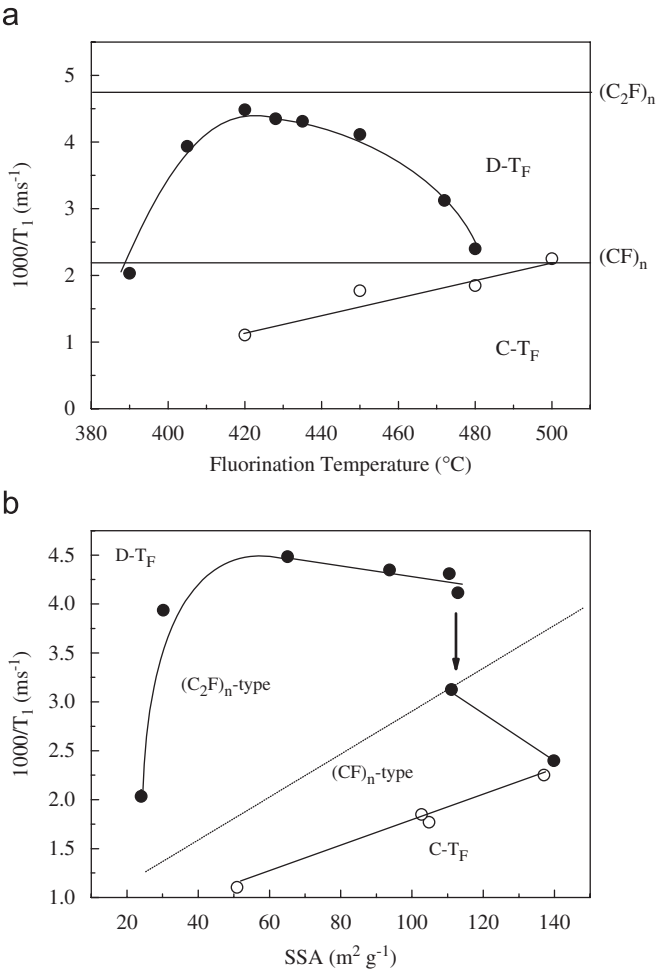

Fig. 8. Evolution of the ^{19}F spin-lattice relaxation rate ($R_1 = 1/T_1$) as a function of the fluorination temperature (a) and of the specific surface area (b).

information. For these two well-known structures, T_1 are equal to 450 and 210 ms, respectively [15,16,18]. In the case of the controlled fluorination for T_F equal to 450, 480 and 500 °C, the T_1 values are in agreement with those of a $(CF)_n$ phase (Fig. 8a and Table 1). For the direct reaction, the T_1 values are close to the one of $(C_2F)_n$ in a wide reaction temperatures range ($420 < T_F < 450\,^{\circ}C$). On the contrary, the T_1 values at the lowest fluorination temperatures significantly differ from the classical values of $(C_2F)_n$ types, which is the main structural phase in these conditions. The same behavior is observed for the controlled route samples i.e. T_1 is higher than the one expected for a $(CF)_n$ type. In both cases, the amount of physisorbed O_2, which is related to the SSA, increases continuously with temperature for $T_F \leqslant 435\,^{\circ}C$. The effect of paramagnetic O_2 is therefore increased resulting in a higher relaxation rate in air atmosphere (all other parameters such as density of DB and structure being quite similar in the compared samples). This clearly appears in Fig. 8b in the initial part of the curve. The same phenomenon explains the higher T_1 value of **C**-420 when compared with **C**-450. These two samples exhibit a SSA of 50.9 ± 0.5 and $104.8 \pm 0.7\,m^2\,g^{-1}$, respectively.

For $435 \leqslant T_F \leqslant 450\,^{\circ}C$ and $T_F = 450$ and 480 °C, respectively for the direct and controlled fluorinations, because the SSA remains nearly constant (Table 1 and Fig. 8), the relaxation rate of the various samples do not change significantly for the two series **D**-T_F and **C**-T_F.

Table 3
Comparison of two covalent graphite fluorides

	T_F (°C)	F:C	T_1 (presence of O_2) (ms)	SSA ($m^2 g^{-1}$)	D_s ($\times 10^{19}$ spin g^{-1})
$(CF)_n$-C	600	1	450	230	1.2
CF-530	25+530[a]	0.92	595	115	0.1

[a] Synthesis at room temperature using $F_{2(g)}$–$HF_{(g)}$–$IF_{5(g)}$ catalytic mixture and a post-fluorination at 530 °C under pure F_2 gas.

Finally, R_1 goes on increasing as the SSA of **C**-500 ($137.2 \pm 0.7\ m^2 g^{-1}$) increases. On the contrary, in the case of direct fluorination, the relaxation rate decreases for the higher T_F although SSA and amount of O_2 are larger. For this reaction temperature, a structural conversion from $(C_2F)_n$ into $(CF)_n$ type occurs; the spin-lattice relaxation time tends towards the typical value of $(CF)_n$-type graphite fluoride ($T_1 = 450$ ms), which is significantly higher than the $(C_2F)_n$ type (210 ms).

In order to definitively prove the effect of adsorbed O_2 molecules, the T_1 values were recorded with out-gassed samples (Table 1); a drastic increase is systematically observed and T_1 reaches a value equal to 1.58 and 1.54 s for **C**-420 and **C**-480, both of $(CF)_n$ structural type. This value can be considered as the intrinsic spin-lattice relaxation time of fluorinated CNFs with this structural stacking. After re-exposure to air atmosphere, the T_1 values are close to the initial values but slightly lower; this effect is probably due to an elimination of both HF and H_2O molecules through out-gassing leading to a total amount of physisorbed O_2 molecules slightly larger than before. The fact that the T_1 values are all very similar proves that the out-gassing process does not modify the chemical nature of the fluorinated CNFs. This is contrary to the case of $(C_2F)_n$-type graphite fluoride whose initial high content of HF molecules is removed by out-gassing [16]. The comparison of the values obtained after out-gassing for **D**-420 and **D**-480 cannot be discussed due to structural conversion.

The values of 1.58 and 1.54 s for CNFs fluorinated using TbF_4 at 420 and 480 °C, respectively, confirm that the fluorocarbon matrix is rigid in accordance with the observed broad ^{19}F NMR line width. The strong correlation of the spin-lattice relaxation rate with the SSA is well highlighted by the case of **C**-T_F compounds (Fig. 8b).

Taking into account the new results in the present paper, previous data about two covalent graphite fluorides with $(CF)_n$ structural type are also discussed: the first sample is conventional $(CF)_n$ obtained at 600 °C starting from petroleum coke (noted $(CF)_n$–C) whereas the second one is prepared using graphite at room temperature with IF_5 catalyst and post-treated at 530 °C (CF-530). For these samples, contrary to the effect of internal paramagnetic center, the effect of paramagnetic oxygen is predominant since the T_1 values increased when the sample were sealed under vacuum [18]. Moreover, although similar structural type and fluorine content ($CF_{0.92}$ for CF-530 and CF_1 for $(CF)_n$–C), T_1 is longer for CF-530 than for $(CF)_n$–C i.e. 595 and 450 ms, respectively (Table 3). The difference between these values are explained by different SSA (50 and 230 $m^2 g^{-1}$ for CF-530 than for $(CF)_n$–C, respectively) and, consequently, the presence of different amounts of physisorbed O_2 molecules; The tendency is similar than for fluorinated CNFs.

4. Conclusion

NMR and EPR characterization allows the fluorination of CNFs using two routes, direct (F_2) and controlled (using TbF_4 as fluorinating agent) to be compared. Whatever the fluorination process a similar structural type is formed: (i) with TbF_4, $(CF)_n$ is present whatever the temperature and (ii) by direct fluorination (using pure F_2 gas), over a wide temperature range ($390 < T_F < 472$ °C), $(C_2F)_n$ is the main phase. The amounts of structural defects, such as DB and CF_2, CF_3 groups, are limited using the controlled process thanks to the progressive release of fluorine during the thermal decomposition of TbF_4. For CNFs fluorinated with TbF_4, the decrease of the defects content associated with a highly fluorinated phase $(CF)_n$ is promising for the use as electrode material in primary lithium battery; their performances in such an application are under investigation.

Moreover, the direct correlation between ^{19}F spin-lattice nuclear relaxation times (T_1) and SSA has been established for fluorinated CNFs. This demonstrates the effect of physisorbed O_2 molecules on the nuclear relaxation since the amount of physisorbed paramagnetic O_2 is related to the SSA. The other parameters which govern the T_1 exhibit low changes i.e. density of DB as internal PC (except after the direct fluorination at 480 °C) and the molecular motion, which is related to the structural type formed, i.e. $(CF)_n$ or $(C_2F)_n$. The presence of atmospheric O_2 definitely influences nuclear relaxation as does the presence of internal DB. Removal of O_2 upon out-gassing results in a longer T_1 value, close to 1.56 s; this value can be considered as the intrinsic spin-lattice relaxation time of fluorinated CNFs having a $(CF)_n$-type structure.

References

[1] T. Nakajima, Synthesis, structure, and physicochemical properties of fluorine–graphite intercalation compounds, in: T. Nakajima (Ed.), Fluorine–Carbon and Fluoride–Carbon Materials, Marcel Dekker, New York, 1995 (Chapter 1).
[2] T. Nakajima, N. Watanabe, Graphite Fluorides and Carbon–Fluorine Compounds, CRC Press, Boca Raton, Ann Arbor, Boston, 1991.
[3] N. Watanabe, T. Nakajima, H. Touhara, Graphite Fluorides, Elsevier, Amsterdam, 1988.
[4] H. Touhara, F. Okino, Carbon 38 (2000) 241–267.
[5] A. Hamwi, J. Phys. Chem. Solids 57 (1996) 677–688.
[6] Y. Sato, K. Itoh, R. Hagiwara, T. Fukunaga, Y. Ito, Carbon 42 (2004) 3243–3249.
[7] Y. Kita, N. Watanabe, Y. Fujii, J. Am. Chem. Soc. 101 (1979) 3832–3841.
[8] R. Yazami, Electrochemical properties of graphite fluorides, metal fluorides, and oxide fluoride GICs, in: T. Nakajima (Ed.), Fluorine–Carbon and Fluoride–Carbon Materials, Marcel Dekker, New York, 1995 (Chapter 7).
[9] A. Hamwi, K. Guérin, M. Dubois, in: Tsuyoshi Nakajima, Henri Groult (Eds.), Fluorine-intercalated graphite for lithium battery in Fluorinated materials for energy conversion, 2005.
[10] R. Yazami, A. Hamwi, K. Guérin, Y. Ozawa, M. Dubois, J. Giraudet, F. Masin, Electrochem. Commun. 9 (2007) 1850–1885.
[11] A.M. Panich, Synthetic Met. 100 (1999) 169–185.
[12] A.M. Panich, A.I. Shames, T. Nakajima, J. Phys. Chem. Solids 62 (2001) 959–964.
[13] T. Mallouk, B.L. Hawkins, M.P. Conrad, K. Zilm, G.E. Maciel, N. Bartlett, Philos. Trans. R. Soc. Lond. A 314 (1985) 179–183.
[14] M. Dubois, K. Guérin, J.-P. Pinheiro, Z. Fawal, F. Masin, A. Hamwi, Carbon 42 (2004) 1931–1940.
[15] J. Giraudet, M. Dubois, A. Hamwi, W.E.E. Stone, P. Pirotte, F. Masin, J. Phys. Chem. B 109 (2005) 175–181.
[16] M. Dubois, J. Giraudet, K. Guérin, A. Hamwi, Z. Fawal, P. Pirotte, F. Masin, J. Phys. Chem. B 110 (2006) 11800–11808.
[17] J. Giraudet, M. Dubois, K. Guérin, C. Delabarre, P. Pirotte, A. Hamwi, F. Masin, Solid State NMR 221 (2007) 131–140.
[18] J. Giraudet, M. Dubois, K. Guérin, A. Hamwi, F. Masin, J. Phys. Chem. Solids 67 (2006) 1100–1105.
[19] J. Giraudet, M. Dubois, K. Guérin, J.-P. Pinheiro, A. Hamwi, W.E.E. Stone, P. Pirotte, F. Masin, J. Solid State Chem. 178 (2005) 1262–1268.
[20] A. Abragam, The Principles of Nuclear Magnetism, Oxford University Press, London, 1961.

[21] W.E. Blumberg, Phys. Rev. 119 (1960) 79–84.
[22] D. Tse, S.R. Hartmann, Phys. Rev. Lett. 21 (1968) 511–514.
[23] M.R. McHenry, B.G. Silbernagel, Phys. Rev. B 5 (1972) 2958–2972.
[24] H. Yokomichi, T. Hayashi, T. Amano, A. Masuda, J. Non-Cryst. Solids 227–230 (1998) 641–644.
[25] H. Yokomichi, K. Morigaki, J. Non-Cryst. Solids 266 (2000) 797–802.
[26] K. Takai, H. Sato, T. Enoki, N. Yoshida, F. Okino, H. Touhara, M. Endo, Mol. Cryst. Liq. Cryst. 340 (2000) 289–294.
[27] S.L. Di Vittorio, T. Enoki, M.S. Dresselhaus, G. Dresselhaus, M. Endo, T. Nakajima, Phys. Rev. B 46 (1992) 12723–12730.
[28] R. Davidov, O. Milo, I. Palchan, H. Selig, Synthetic Met. 8 (1983) 83–87.
[29] F. Chamssedine, M. Dubois, K. Guérin, J. Giraudet, F. Masin, D.A. Ivanov, L. Vidal, R. Yazami, A. Hamwi, Chem. Mater. 19 (2007) 161–172.
[30] N.S. Chilingarov, J.V. Rau, L. Sidorov, N.L. Bencze, A. Popovic, V.F. Sukhoverkhov, J. Fluorine Chem. 104 (2000) 291–295.
[31] J. Giraudet, M. Dubois, K. Guerin, C. Delabarre, A. Hamwi, F. Masin, J. Phys. Chem. B 111 (51) (2007) 14143–14151.
[32] Y. Sato, K. Itoh, R. Hagiwara, T. Fukunaga, Y. Ito, Carbon 42 (14) (2004) 2897–2903.
[33] C.A. Wilkie, G.Y. Lin, D.T. Haworth, J. Solid State Chem. 30 (1979) 197–201.
[34] F. Chamssedine, D. Claves, Chem. Phys. Lett. 454 (2008) 252–256.
[35] J.C. Scott, P. Pfluger, M.T. Krounbi, G.B. Street, Phys. Rev. B 28 (1983) 2140.
[36] V.I. Krinichnyi, H.-K. Roth, M. Schrödner, B. Wessling, Polymer 47 (2006) 7460–7468.
[37] V.I. Krinichnyi, S.V. Tokarev, H.-K. Roth, M. Schrödner, B. Wessling, Synthetic Met. 156 (21–24) (2006) 1368–1377.
[38] El M. Moujahid, M. Dubois, J.-P. Besse, F. Leroux, Chem. Mater. 14 (2002) 3799–3807.